Mass Dependence and Finite Observation Window Effects in Eccentric Equatorial EMRI Waveforms

Junyi Zhang[1], **Jingxu Wu**[2,*]

[1]Faculty of Computational Mathematics and Cybernetics, Lomonosov Moscow State University, Moscow 119991, Russia • [2]Faculty of Physics, Lomonosov Moscow State University, Moscow 119991, Russia

Poster Sheet 1 / 5

Corresponding: wuxj@my.msu.ru

Framework: FastEMRIWaveforms v2.2.0
Total Scope: 264 Runs + 21 Phase Checks

1. EXECUTIVE ABSTRACT & PHYSICAL MOTIVATION

Abstract (EN): Finite observation windows can obscure leading mass scaling in extreme-mass-ratio inspirals (EMRIs). Using `FastEMRIWaveforms` (FEW) v2.2.0 [1–4], we calculate 30 eccentric equatorial inspirals into spinning Kerr black holes with primary masses $m_1 \in \{1, 2, 5\} \times 10^6\ M_\odot$ and secondary masses $m_2 \in \{1, \ldots, 10\}\ M_\odot$ over a fixed physical window $T = 0.01$ yr. We fit the RMS strain $A_{\rm rms}$ and mean azimuthal orbital frequency $\bar{f}_\varphi$, retain the total-mass ($M = m_1 + m_2$) initial-frequency shift in the phase model $\Delta\Phi_\varphi$, test predictions across 38 external mass pairs (18 development + 20 blind holdout), and run scaled-window duration controls at $m_1 \in \{30, 80, 150\} \times 10^6\ M_\odot$.

Аннотация (RU): С помощью FastEMRIWaveforms v2.2.0 сравниваются 30 вариантов эксцентрического экваториального спирального сближения с чёрной дырой Керра при m_1 = (1, 2, 5) × 10^6 $M_\odot$ и m_2 = 1–10 $M_\odot$ на окне T = 0.01 года. Контрольные расчёты с масштабированной длительностью уменьшают максимальное отклонение RMS-амплитуды при больших массах с 6.285% до 0.02816%.

- **Leading Analytic Scaling vs. Finite-Window Bias:** While FEW mode amplitudes normalize strain by the reduced mass ($A_{\rm rms} \propto m_2$) and physical frequencies by the inverse total mass ($\bar{f}_\varphi \propto M^{-1}$) [2], a fixed physical window samples a primary-mass-dependent number of orbital cycles (from **355.6 cycles** at $10^6\ M_\odot$ down to **2.37 cycles** at $1.5 \times 10^8\ M_\odot$).
- **Connection to Detector-Weighted EMRI Inference:** Separating window-truncation artifacts and mass conventions from genuine physical dephasing is essential before evaluating post-adiabatic corrections [5] or localized dissipative flux transitions in detector-weighted LISA likelihood analyses [6].

Table 1. Source Parameters & Production Settings in FEW v2.2.0

Quantity / Setting	Production Value & Convention
Waveform Model	`FastKerrEccentricEquatorialFlux`, FEW v2.2.0 (CPU execution) [2–4]
Baseline Primary Mass m_1	(1, 2, 5) × $10^6\ M_\odot$ (model inputs; no cosmological redshift applied)
Baseline Secondary Mass m_2	1, 2, 3, 4, 5, 6, 7, 8, 9, 10 $M_\odot$ (30 baseline mass pairs)
Dimensionless Spin & Orbit	$a = 0.9$, $p_0 = 8.5$, $e_0 = 0.3$, $x_0 = +1$ (prograde equatorial orbit)
Distance & Source Angles	$D = 1$ Gpc; $\theta_S = \varphi_S = \theta_K = \varphi_K = \pi/3$ (two-polarization source strain)
Initial Orbital Phases	$\Phi_\varphi(0) = \Phi_r(0) = \pi/3$; $\Phi_\theta(0) = 0$
Evolution & Sampling	$T = 0.01$ yr = 315,581.4976 s (≈ 87.66 h); $\Delta t = 5$ s (N = 63,117 samples)
Numerical Convergence Controls	Harmonic mode threshold 10^{-8}; ODE trajectory relative tolerance 10^{-12}

2. CONTROLLED MASS COMPARISON ON THE 30-POINT GRID

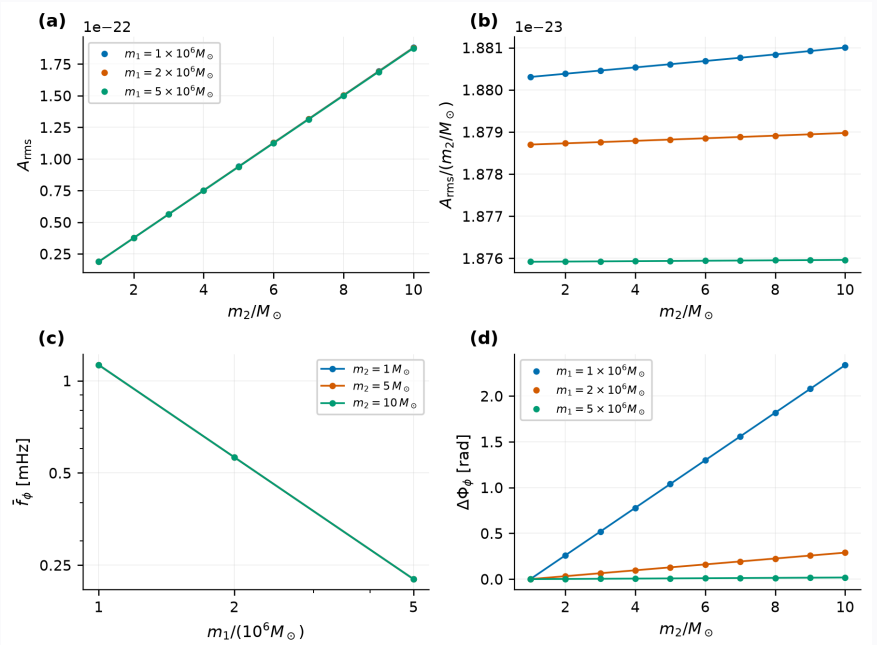


Fig. 1. Mass dependence on the original 30-point training grid: (a) Two-polarization RMS strain $A_{\rm rms}$ and power-law curves vs. m_2; (b) secondary-mass-normalized strain $A_{\rm rms}/(m_2/M_\odot)$ revealing weak residual offsets across primary-mass groups; (c) mean orbital azimuthal frequency $\bar{f}_\varphi$ at fixed m_2; (d) accumulated azimuthal phase difference $\Delta\Phi_\varphi$ relative to the 1 $M_\odot$ reference at the same primary mass.

Table 3. Selected Baseline Benchmarks at $m_2 = 10\ M_\odot$ ($T = 0.01$ yr)

Primary Mass $m_1 / 10^6\ M_\odot$	$A_{\rm rms} / 10^{-22}$	$\bar{f}_\varphi$ [mHz]	Azimuthal Cycles in T	$\Delta\Phi_\varphi$ [rad] (vs. 1 $M_\odot$)
1.0	1.881004	1.1267894	355.59	2.3401738
2.0	1.878976	0.5629014	177.64	0.2894940
5.0	1.875963	0.2251058	71.04	0.0180365

Key Baseline Findings: Across the 30-point grid, $A_{\rm rms}$ curves nearly coincide at equal m_2, while dividing by m_2 exposes a weak ~0.27% shift between $m_1 = 10^6$ and $5 \times 10^6\ M_\odot$ caused by slower radiative evolution and fewer sampled cycles over the fixed 0.01-yr window.

Key Reference: J. Wu *et al.*, *Class. Quantum Grav.* **43**(17), doi:10.1088/1361-6382/ae9e7c (2026)

Full Observation-Window Waveforms (T = 0.01 yr = 87.66 h) & Multi-Harmonic Dephasing

Junyi Zhang[1], Jingxu Wu[2,*]

[1]Faculty of Computational Mathematics and Cybernetics, Lomonosov Moscow State University • [2]Faculty of Physics, Lomonosov Moscow State University

3. FULL-WINDOW STRAIN WAVEFORMS ($T \in [0, 87.66\ \mathrm{H}]$)

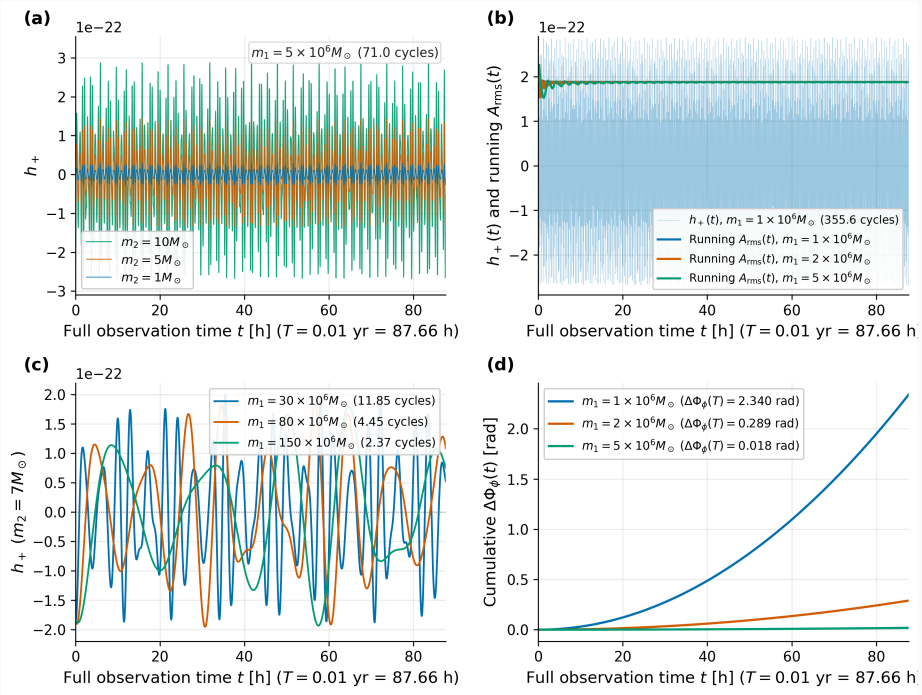


Fig. 2A. Full observation-window waveform diagnostics over T = 0.01 yr (87.66 h): (a) Complete 87.66-h plus-polarization strain $h_+(t)$ at m_1 = 5 × 10^6 $M_\odot$ (71.0 azimuthal cycles) for m_2 = 1, 5, 10 $M_\odot$; (b) dense carrier and cumulative running RMS $A_{\mathrm{rms}}(t)$ across m_1 = (1, 2, 5) × 10^6 $M_\odot$ demonstrating rapid convergence above ~30 cycles; (c) full-window high-mass waveforms at m_1 = (30, 80, 150) × 10^6 $M_\odot$ (m_2 = 7 $M_\odot$), showing how 150 × 10^6 $M_\odot$ spans only **2.37 azimuthal cycles**; (d) quadratic-in-time cumulative dephasing $\Delta\Phi_\varphi(t)$ reaching 2.340, 0.289, and 0.018 rad at t = 87.66 h.

- **Why Full-Window Inspection Matters:** Over the complete T = 87.66 h interval, eccentric Kerr waveforms exhibit strong periastron-precession amplitude modulation (interference of azimuthal harmonics m and radial harmonics n at frequencies $m\Omega_\varphi + n\Omega_r$).
- **Origin of High-Mass RMS Departure:** Panel (c) directly shows why the fixed 87.66-h window produces a −6.285% RMS shift at m_1 = 1.5 × 10^8 $M_\odot$: sampling only 2.37 azimuthal cycles leaves the discrete time average sensitive to boundary phase placement rather than secular inspiral amplitude evolution.

4. EARLY- VS. LATE-TIME WAVEFORM ZOOM COMPARISON

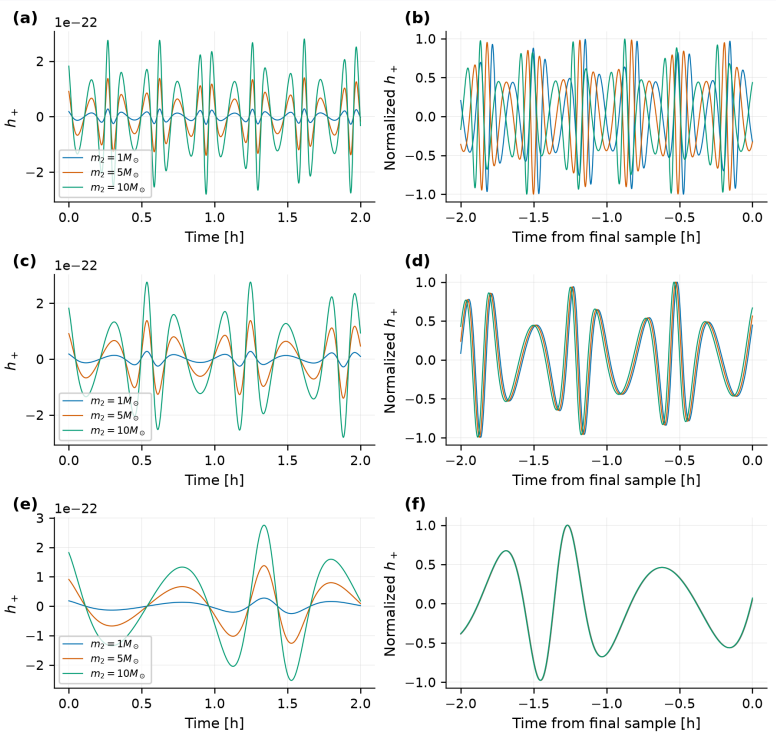


Fig. 2B. Early- and late-time waveform segments across m_1 = (1, 2, 5) × 10^6 $M_\odot$: Plus-polarization strain h_+ at m_1 = 10^6 $M_\odot$ (a,b), 2 × 10^6 $M_\odot$ (c,d), and 5 × 10^6 $M_\odot$ (e,f) for m_2 = 1, 5, 10 $M_\odot$. Left panels (a,c,e) show the first 2 h of physical strain; right panels (b,d,f) show the final 2 h normalized by each segment's maximum $|h_+|$.

- **Amplitude vs. Phase Separation:** Left panels (a, c, e) confirm linear amplitude scaling with m_2 while all curves begin in phase at t = 0. Right panels (b, d, f) isolate cumulative dephasing over [85.66 h, 87.66 h]: strong waveform dephasing appears at m_1 = 10^6 $M_\odot$ (b), moderate shift at 2 × 10^6 $M_\odot$ (d), and near-exact overlap at 5 × 10^6 $M_\odot$ (f).
- **Multi-Harmonic Structure:** Because an eccentric waveform sums many relativistic (l, m, k, n) modes, peak displacement in normalized h_+ does not define a single harmonic phase—motivating the exact orbital azimuthal diagnostics $\bar{f}_\varphi$ and $\Delta\Phi_\varphi$.

Key Reference: J. Wu *et al.*, *Class. Quantum Grav.* **43**(17), doi:10.1088/1361-6382/ae9e7c (2026)

Discrete Waveform Observables, Empirical Power-Law Fits & Precision Controls

Junyi Zhang[1], Jingxu Wu[2,*]

[1]Faculty of Computational Mathematics and Cybernetics, Lomonosov Moscow State University • [2]Faculty of Physics, Lomonosov Moscow State University

Mode Threshold: 10^{-8} (δRMS = 0.0027%)
ODE Tolerance: 10^{-12} ($L_2 = 4.22\times10^{-8}$)
Duration Scaling: $\Delta\Phi_{evol} \propto T^{2.000–2.005}$

5. OBSERVABLES & EMPIRICAL POWER-LAW MODELS

We define the discrete two-polarization RMS strain across all N samples (Eq. 1), the mean orbital azimuthal frequency over the evolution window T (Eq. 2), and the accumulated azimuthal phase shift relative to a 1 $M_\odot$ secondary at the same primary mass (Eq. 3):

$$A_{\rm rms} = [\, N^{-1} \Sigma_{j=1..N} (h_{+,j}^{\,2} + h_{\times,j}^{\,2}) \,]^{1/2} \quad (1)$$

$$\Psi_\varphi = \Phi_\varphi(T) - \Phi_\varphi(0), \quad \bar{f}_\varphi = \Psi_\varphi / (2\pi T) \quad (2)$$

$$\Delta\Phi_\varphi(m_1, m_2) = \Psi_\varphi(m_1, m_2) - \Psi_\varphi(m_1, 1\,M_\odot) \quad (3)$$

Setting dimensionless mass variables $x = m_1/(10^6\,M_\odot)$ and $u = m_2/M_\odot$, we fit the positive amplitude and frequency across the 30-point grid via unweighted least squares in logarithmic space:

$$y(m_1, m_2) = C \cdot x^b \cdot (u/10)^a \quad (4)$$

Table 2. Empirical Fits to the Final 30-Point Baseline Grid (Eq. 4)

Observable y	Coefficient C	Primary Exponent b	Secondary Exponent a	Leading Analytic Scale
$A_{\rm rms}$ [strain]	1.880848×10^{-22}	−0.0015641	1.0000783	$\propto m_1^{\,0}\, m_2^{\,1}$
$\bar{f}_\varphi$ [Hz]	1.126282×10^{-3}	−1.0003700	0.0001962	$\propto m_1^{\,-1}\, m_2^{\,0}$

Table 4. Largest Differences in Final Numerical Convergence Checks

Convergence Check (7 Representative Mass Pairs)	Maximum Observed Numerical Difference
Harmonic mode threshold 10^{-8} vs. 10^{-9}	RMS diff. **0.002702%**; unweighted mismatch 6.29×10^{-9}
Time sampling step Δt = 5 s vs. 1.25 s	RMS diff. **0.000244%**; common-time samples agree to machine precision
Trajectory ODE tolerance 10^{-12} vs. 10^{-13}	Relative waveform L_2 norm difference **4.22×10^{-8}**; $\lvert\delta\Phi_\varphi\rvert \le 2.83 \times 10^{-8}$ rad

Solver vs. Physical Approximation Scope: An initial quick scan at mode threshold 10^{-2} underestimated $A_{\rm rms}$ by 4.59%, and 10^{-6} remained above the 0.02% target; all 264 production runs therefore enforce 10^{-8}. While Table 4 bounds internal numerical sensitivity within FEW v2.2.0, physical waveform faithfulness in LISA data analysis additionally requires first post-adiabatic (1PA) self-force terms [5] and detector-weighted residual & profile-likelihood assessments of localized dissipative phase transitions [6].

6. NUMERICAL SENSITIVITY & DURATION SCALING CHECKS

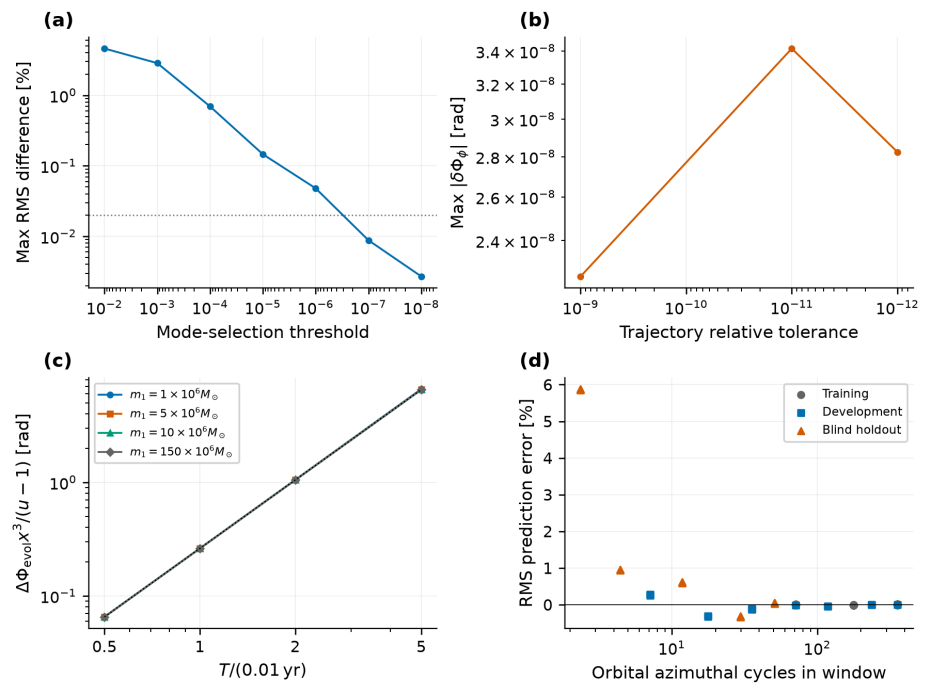


Fig. 3. Numerical convergence and duration scaling checks: (a) Maximum RMS difference across seven representative mass pairs relative to mode threshold 10^{-9} (dotted line marks the 0.02% numerical target); (b) accumulated orbital-phase differences $|\delta\Phi_\varphi|$ relative to trajectory ODE tolerance 10^{-13}; (c) mass-normalized radiative evolution phase $\Delta\Phi_{evol}\, x^3/(u-1)$ across $T \in \{0.005, 0.01, 0.02, 0.05\}$ yr confirming the quadratic T^2 adiabatic accumulation law; (d) RMS prediction error vs. number of azimuthal orbital cycles in the fixed 0.01-yr window.

- **Quadratic Time Accumulation (Panel c):** Across T = 0.005, 0.01, 0.02, and 0.05 yr, subtracting the initial-frequency offset yields a universal time exponent between **2.000 and 2.005** across all primary masses (10^6 to 1.5×10^8 $M_\odot$), matching leading short-window secular frequency drift $\Delta\Phi_{evol} \approx \tfrac{1}{2}(2\pi\dot{f}_\varphi)T^2$.
- **Cycle-Count Threshold for RMS Stability (Panel d):** Prediction errors remain below 0.35% whenever the window contains ≥ 15 azimuthal cycles, rising sharply only when cycle count drops below ~10 cycles at high m_1.

Key Reference: J. Wu *et al.*, *Class. Quantum Grav.* **43**(17), doi:10.1088/1361-6382/ae9e7c (2026)

Phase Extrapolation, Total-Mass Convention ($M = m_1 + m_2$) & Zero-Crossing Controls

Junyi Zhang[1], **Jingxu Wu**[2,*]

[1]Faculty of Computational Mathematics and Cybernetics, Lomonosov Moscow State University • [2]Faculty of Physics, Lomonosov Moscow State University

Phase Fit: C_φ = 0.261980 rad, b_φ = −3.000855

Sign Reversal: 1.1458–1.1925 × 10^8 $M_\odot$

Quadrature Precision: 2.27 × 10^{-12} rad

7. TOTAL-MASS 0PA FREQUENCY CONVENTION & PHASE DECOMPOSITION

In FEW v2.2.0, the physical 0PA orbital azimuthal frequency is normalized by the **total mass** $M = m_1 + m_2$ rather than m_1 alone [2, 4]:

$$f_0(m_1, m_2) = \Omega_\varphi(a, p_0, e_0, x_0) / [\, 2\pi\, (m_1 + m_2)\, t_\odot \,], \quad t_\odot = GM_\odot / c^3 \quad (5)$$

When m_1 is held fixed and m_2 increases from 1 $M_\odot$ to u $M_\odot$, the heavier secondary slightly *lowers* the initial orbital frequency f_0, contributing a negative linear-in-T phase shift ($\propto m_1^{-2}$). Subtracting this exact analytical initial-frequency shift isolates the positive adiabatic radiation-reaction evolution term ($\propto m_1^{-3}$):

$$\Delta\Phi_\varphi(m_1, m_2) \approx 2\pi T\, [\, f_0(m_1, m_2) - f_0(m_1, 1\, M_\odot) \,] + C_\varphi\, (u - 1)\, x^{b_\varphi} \quad (6)$$

Fitting the 27 non-reference training pairs yields $\boldsymbol{C_\varphi = 0.2619796}$ **rad** and $\boldsymbol{b_\varphi = -3.0008554}$ at T = 0.01 yr.

Why Single Power Laws Fail at High Primary Mass

- **Single Power-Law Breakdown:** Fitting $\Delta\Phi_\varphi$ directly without subtracting the f_0 shift gives $0.2603799(u - 1)x^{-3.022987}$ rad on the training grid, but suffers a **59% prediction error** on the development set at $m_1 = 5 \times 10^7$ $M_\odot$ and >300% at 1.5×10^8 $M_\odot$ (Fig. 4b).
- **Competing Mass Scalings & Smooth Sign Reversal:** Because the positive radiation-reaction term decays as x^{-3} while the negative initial-frequency offset decays as x^{-2}, the two terms cancel smoothly between **1.1458×10^8 $M_\odot$ and 1.1925×10^8 $M_\odot$** for T = 0.01 yr (Fig. 4c).
- **Fixed-m_1 vs. Fixed-Total-Mass Controls (Fig. 4d):** Adjusting m_1 by $(1 - u)$ $M_\odot$ so that $M = m_1 + m_2$ stays strictly constant eliminates the f_0 shift. At anchor mass 1.5×10^8 $M_\odot$ (m_2 = 10 $M_\odot$), direct FEW evaluation gives **-1.95×10^{-7} rad** at fixed m_1 versus **$+6.97 \times 10^{-7}$ rad** at fixed total mass M.
- **High-Precision Quadrature Verification (21 Checks):** Near the zero crossing, direct subtraction of large accumulated phases loses floating-point precision. Integrating the exact orbital-frequency difference via 1025- and 2049-point Simpson quadrature under stricter ODE tolerances confirms stability to **2.27×10^{-12} rad**.

8. PHASE EXTRAPOLATION & MASS-CONVENTION CONTROLS

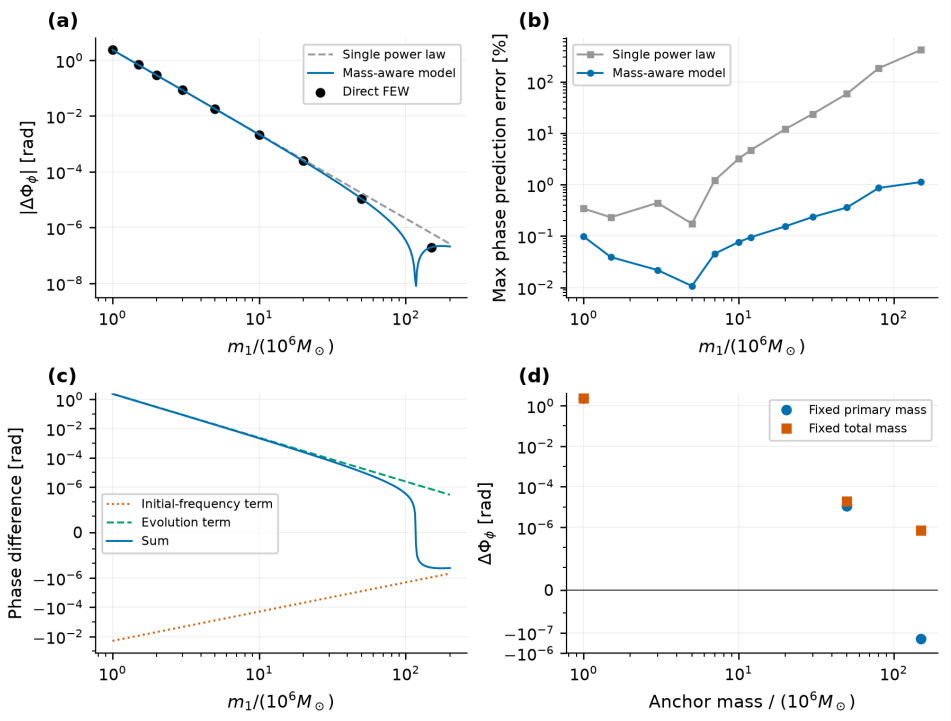


Fig. 4. Phase extrapolation and mass-convention controls: (a) Absolute phase differences $|\Delta\Phi_\varphi|$ at m_2 = 10 $M_\odot$ comparing a single power law (dashed grey), the mass-aware model of Eq. 6 (solid blue), and direct FEW evaluations (black circles); (b) maximum phase prediction error across primary masses showing the >100× accuracy improvement of Eq. 6 above 10^7 $M_\odot$; (c) signed decomposition into the negative initial-frequency term (dotted orange), positive adiabatic evolution term (dashed green), and their net sum (solid blue); (d) direct FEW controls for m_2 = 1 → 10 $M_\odot$ under fixed primary mass m_1 (blue circles, sign flip at 1.5×10^8 $M_\odot$) versus fixed total mass $M = m_1 + m_2$ (orange squares, strictly positive).

Key Reference: J. Wu *et al.*, *Class. Quantum Grav.* **43**(17), doi:10.1088/1361-6382/ae9e7c (2026)

External Holdout Validation (68 Pairs), Scaled-Window Controls & LISA Synthesis

Junyi Zhang[1], Jingxu Wu[2,*]
[1]Faculty of Computational Mathematics and Cybernetics, Lomonosov Moscow State University • [2]Faculty of Physics, Lomonosov Moscow State University

9. EXTERNAL PREDICTION VALIDATION ACROSS 68 MASS PAIRS

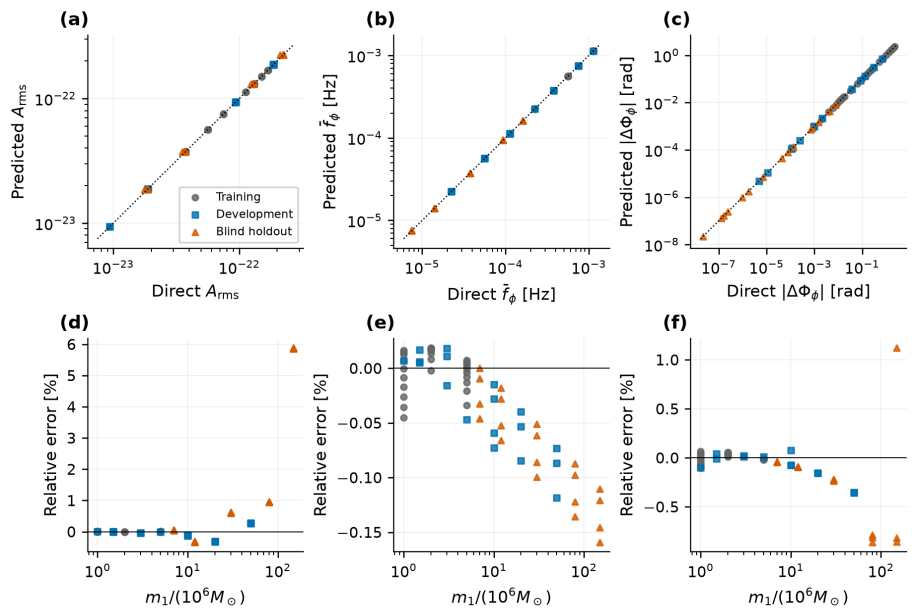


Fig. 5. Training, development, and blind holdout validation: Grey circles show the 30 training pairs; blue squares show 18 development pairs ($m_1 \in \{1.5, 3, 10, 20, 50\} \times 10^6\ M_\odot$, $m_2 \in \{1, 5, 10\}\ M_\odot$ plus 3 subsolar tests at 0.5 $M_\odot$); orange triangles show 20 blind holdout pairs ($m_1 \in \{7, 12, 30, 80, 150\} \times 10^6\ M_\odot$, $m_2 \in \{1, 2, 7, 12\}\ M_\odot$). Max blind-holdout absolute phase error is 3.56×10^{-6} rad.

Table 5. Largest Absolute Relative Prediction Errors Across Datasets

Predicted Quantity	Training (30)	Development (18)	Blind Holdout (20)
RMS Strain A_{rms} (Eq. 4)	0.01223%	0.3247%	**5.879%**
Mean Orbital Frequency $\bar{f}_\varphi$ (Eq. 4)	0.04503%	0.1185%	**0.1590%**
Corrected Phase Difference $\Delta\Phi_\varphi$ (Eq. 6)	0.1044%	0.3585%	**1.120%**

10. SCALED-WINDOW CONTROLS & SYNTHESIS WITH WU *ET AL.* (2026 CQG)

To isolate the cause of the 5.879% holdout A_{rms} departure at $m_1 = 1.5 \times 10^8\ M_\odot$, we ran six scaled-window controls at $m_1 \in \{30, 80, 150\} \times 10^6\ M_\odot$ ($m_2 \in \{1, 7\}\ M_\odot$) where both physical duration T and sampling step Δt are multiplied by $m_1/(10^6\ M_\odot)$, preserving ~355.6 dimensionless orbital cycles:

Table 6. High-Mass RMS Departures from $10^6\ M_\odot$ Reference (m_2 = 1 and 7 $M_\odot$)

Primary Mass m_1 / $10^6\ M_\odot$	Fixed Physical Window (T = 0.01 yr)	Scaled Window (T, $\Delta t \propto m_1$)	Error Reduction
30	−1.136% to −1.112%	**−0.02738% to −0.00397%**	41× – 280×
80	−1.626% to −1.602%	**−0.02799% to −0.00406%**	58× – 395×
150	−6.285% to −6.262%	**−0.02816% to −0.00409%**	**223× – 1530×**

- **Resolution of High-Mass Amplitude Departure:** Scaling T and Δt with m_1 reduces the peak RMS departure from **6.285% to 0.02816%**, confirming that apparent high-mass amplitude deviations in fixed-time scans are dominated by finite-window cycle truncation.
- **Synthesis with Detector-Weighted Transition Signatures (Wu *et al.*, CQG 2026 [6]):** In *Class. Quantum Grav.* **43**(17) (2026), **J. Wu** *et al.* demonstrated that localized dissipative flux transitions in Kerr EMRIs ($M = 2\times10^5\ M_\odot$, $\mu = 1.4\ M_\odot$, $\hat{a} = 0.90$) can maintain high global overlap (extrinsic mismatch 4.828×10^{-3}, refit mismatch 5.95×10^{-8}) while generating substantial detector-weighted residuals ($\rho_R = 2.948$ at $\rho_B = 30$) and systematic intrinsic parameter biases ($\Delta M/M = -3.32\times10^{-5}$, $\Delta\mu/\mu = +2.11\times10^{-5}$, $\Delta\hat{a} = -1.34\times10^{-6}$; Asimov profile likelihood $\Delta\chi^2 = 8.67$). Together, our finite-window mass-scaling baseline and the detector-weighted framework of Wu *et al.* [6] provide a rigorous foundation for disentangling convention and window artifacts from genuine strong-field physics in LISA inference.

References

[1] M. L. Katz, A. J. K. Chua, L. Speri, N. Warburton, and S. A. Hughes, *Phys. Rev. D* **104**, 064047 (2021).

[2] C. E. A. Chapman-Bird *et al.*, *Phys. Rev. D* **112**, 104023 (2025).

[3] J. Zhang and J. Wu, *Mass Dependence and Finite Observation Window Effects in Eccentric Equatorial EMRI Waveforms* (2026).

[4] Black Hole Perturbation Toolkit, *FEW v2.2.0 Docs* & Zenodo (2026).

[5] O. Burke *et al.*, *Phys. Rev. D* **109**, 124048 (2024).

[6] **J. Wu**, L. Luo, J. Yang, H. Ma, and J. Shi, "Detector-weighted signatures of localized dissipative transitions in Kerr EMRIs," *Class. Quantum Grav.* **43**(17), doi:10.1088/1361-6382/ae9e7c (2026).